ORIGINAL ARTICLE

WO$_3$ mesocrystal-assisted photoelectrochemical activity of BiVO$_4$

Chien Nguyen Van[1], Thi Hien Do[2], Jhih-Wei Chen[3], Wen-Yen Tzeng[4], Kai-An Tsai[1], Haili Song[5], Heng-Jui Liu[6], Yan-Cheng Lin[4], Yi-Chun Chen[3], Chung-Lin Wu[3], Chih-Wei Luo[4], Wu-Ching Chou[4], Rong Huang[5], Yung-Jung Hsu[1] and Ying-Hao Chu[1,2,4,5]

Self-assembled nanocomposites have gained much attention over the past decade due to their intriguing properties and functionalities. In this work, we developed a self-assembled nanocomposite photoanode composed of an epitaxial BiVO$_4$ matrix embedded with WO$_3$ mesocrystals for photoelectrochemical (PEC) applications in the visible-light regime. The orientation of the crystal facet and interface provides a superior template to understand the intimate contact between the two constituent phases. We demonstrate that the interfacial coupling of the mesocrystal and matrix improves the separation of photoexcited carriers and the properties of charge transfer, resulting in a greatly enhanced PEC performance compared with their parent compounds. The current study demonstrates that the utilization of the interface-to-volume ratio to optimize charge interactions in the nanocomposite is essential for the advanced design of novel mesocrystal-embedded nanocomposite photoelectrodes.
NPG Asia Materials (2017) **9**, e357; doi:10.1038/am.2017.15; published online 10 March 2017

INTRODUCTION

Photoelectrochemical (PEC) water splitting is the most advanced technology to convert solar energy, an abundant source of energy, into storable and friendly environmental energy in the form of hydrogen.[1,2] The current direction along this research field focuses on the development of new photocatalyst structures with high-efficiency photoconversion, wide absorption of the solar spectrum and stability in electrolyte. Although various single-phase photocatalysts show PEC activities, there still remain critical obstacles to be solved before practical application. For instance, single-phase photocatalysts with suitable bandgaps can capture visible light; however, they are prone to photocorrosion, whereas others show good stability but insufficient absorption of solar light due to their large bandgaps.[3] To overcome the limitations of single-phase photocatalysts, the use of nanocomposites consisting of various phases in the nanoscale has drawn significant attention.[4] For example, by combining photocatalysts with different bandgaps, the utilization of solar energy can be more efficient in nanocomposite systems. The formation of a heterojunction improves charge transport and leads to photocatalysts with better efficiency. One critical obstacle in the path of studying interface coupling in the desired heterojunction is a lack of control of the physical contact between the constituent phases. Unfortunately, obtaining a controllable interface at the atomic level within the nanocomposites remains a great challenge. In addition, researchers have demonstrated that charge transfer and photoactivity are strongly related to the exposed crystal facet of the photocatalysts,[5–7] which increases the difficulty in understanding the system clearly. Recently, mesocrystal systems composed of orientationally aligned functional nanocrystals have drawn much attention, because these superstructures can exhibit new functionalities due to their large surface-to-volume ratio compared with that of single crystals.[8,9] Furthermore, through epitaxial growth, the mesocrystals can be embedded into an epitaxial matrix to form a new nanocomposite photoelectrode with precise control of the film orientation, a well-defined interface between constituent phases and the preclusion of unexpected factors, such as structural defects, grain boundaries and impurity phases. Intimate contact between the mesocrystal and matrix with a high interface-to-volume ratio promotes a strong interfacial interaction, resulting in various intriguing phenomena, such as tunable magnetic anisotropy, enhanced magnetoresistance[10] and permanent ferroelectric retention. Therefore, in this study, we attempt to use the mesocrystal-embedded system as a template to obtain a fundamental understanding of nanocomposite systems. Such a model system can not only acquire critical information about the designed hybrid structures but also provide a new architecture to explore material systems for PEC applications.

[1]Department of Materials Science and Engineering, National Chiao Tung University, Hsinchu, Taiwan; [2]Institute of Physics, Academia Sinica, Taipei, Taiwan; [3]Department of Physics, National Cheng Kung University, Tainan, Taiwan; [4]Department of Electrophysics, National Chiao Tung University, Hsinchu, Taiwan; [5]Key Laboratory of Polar Materials and Devices, Ministry of Education, East China Normal University, Shanghai, China and [6]Department of Material Science and Engineering, National Chung Hsing University, Taichung, Taiwan
Correspondence: Professor Y-H Chu, Department of Materials Science and Engineering, National Chiao Tung University, Room 709, Engineering Building VI, 1001 University Road, Hsinchu 30010, Taiwan, ROC.
E-mail: yhc@nctu.edu.tw

2

One decisive factor in the photoactivity of nanocomposite systems is charge migration across the heterointerfaces, contributed by the charge separation of photoexcited carriers. Hence, an in-depth understanding of charge separation in the heterojunction is essential to the design of PEC structures with high efficiency. A direct bandgap of ~ 2.5 eV together with desirable band edges, good stability and a theoretical solar-to-hydrogen conversion efficiency of 9.2% with a maximum photocurrent of 7.5 mA cm^{-2} makes BiVO$_4$ (BVO) one of the most promising photocatalysts for the evolution of O$_2$ in PEC water splitting.[11,12] However, the performance of its photoactivity is limited by its moderate charge transport properties. Therefore, in this study, we adopt an epitaxial BVO film as the parent compound. In addition, WO$_3$ (WO) is an attractive photocatalyst due to its low cost, environmental friendliness, high chemical stability and good charge transport properties;[13] thus, it could be an ideal material to couple with BVO to improve the photoactivity.[14–16] In this work, in order to explore the charge interaction of oxide heterostructures, we studied a self-assembled mesocrystal-embedded system composed of WO and BVO phases, as illustrated in Figure 1. The photoactivity of the mesocrystal-embedded heterostructure can be greatly improved, as shown through a detailed investigation of the structural features, band alignment and PEC performance. This improvement is attributed to charge interactions at the heterojunction, as evidenced by a combination of X-ray photoelectron spectroscopy (XPS), ultrafast dynamics analysis, photoluminescence (PL) spectroscopy and electrochemistry impedance spectroscopy (EIS).

MATERIALS AND METHODS

The WO–BVO heterostructure films were deposited by pulsed laser deposition at 600 °C in 150 mTorr of oxygen using a dual target (BVO and WO) system. The volume fraction of the two phases was controlled by adjusting the number of laser pulses hitting each target. The thickness of the films was controlled by the number of repetitions. The growth rate for BVO and WO were approximately 0.1 and 0.12 Å per pulse, respectively. The conducting layer Indium tin oxide (ITO) was epitaxially grown on YSZ (100) by pulsed laser
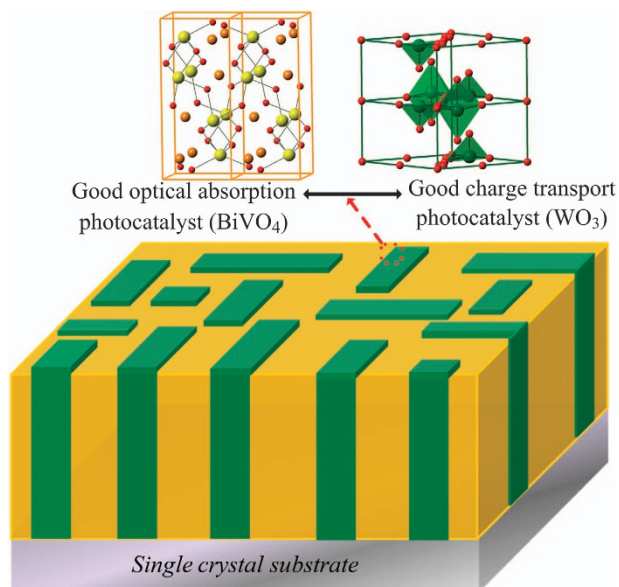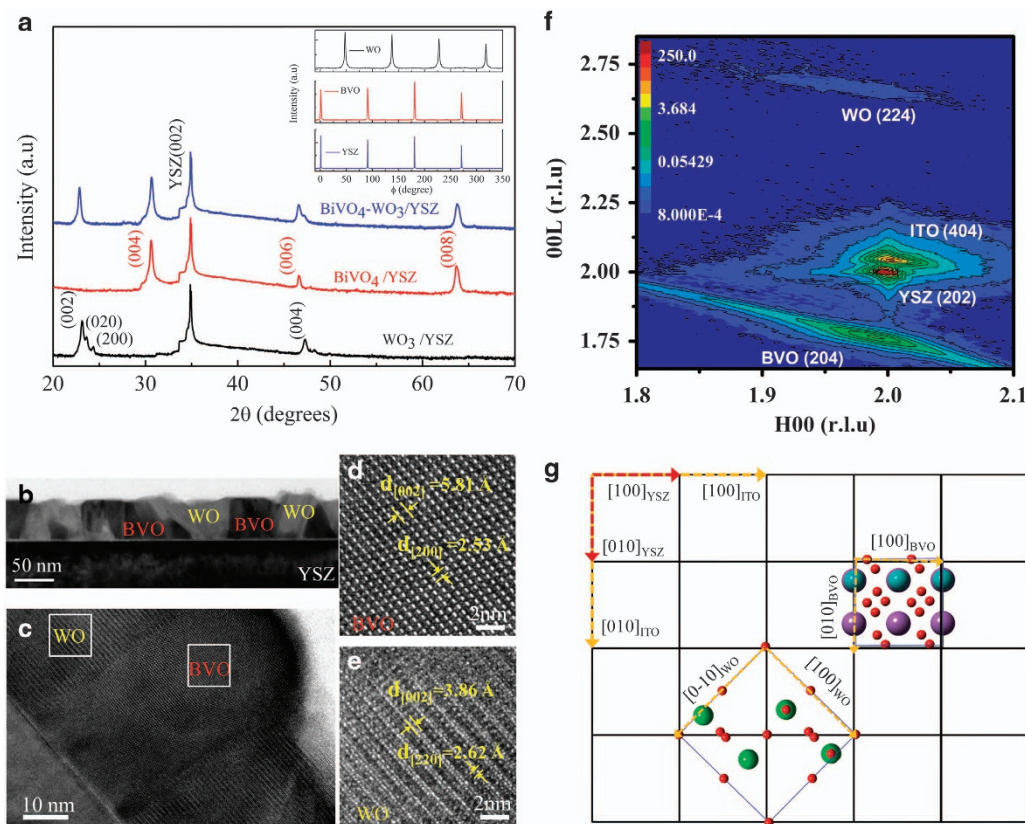
deposition at 400 °C under an oxygen pressure of 10^{-3} Torr. The detailed microstructure and crystallinity of the films were investigated by a JEM-2100F (JEOL, Tokyo, Japan) transmission electron microscope (TEM) and X-ray diffraction (XRD). The energy band alignment of the heterostructure was investigated by XPS. The femtosecond spectroscopy measurement was performed using a dual-color pump–probe system with a commercial Ti:sapphire laser (repetition rate: 5.2 MHz, wavelength: 800 nm, pulse duration: 70 fs) and the standard lock-in technique. The power of the pump beam and the probe beam are 10 and 1 mW, respectively. PL was excited using a He-Cd laser (325 nm) at 10 K. Signals were dispersed using a Horiba iHR550 spectrometer (Horiba, Tokyo, Japan) with a 2400 g mm^{-1} grating and detected using a multichannel liquid-nitrogen (LN$_2$) two-cooled charge-coupled device. EIS was performed in 0.5 M Na$_2$SO$_4$ aqueous solution at 0.6 V versus Ag/AgCl under AM 1.5 illumination. The amplitude of the sinusoidal wave was set at 10 mV, whereas the frequency varied from 100 kHz to 1 Hz.

PEC measurements were conducted using a three-electrode cell with Ag/AgCl as the reference electrode, a Pt counter electrode and 0.5 M Na$_2$SO$_4$ electrolyte. The WO–BVO photoelectrode was grown on a YSZ substrate with an ITO conducting buffer layer. PEC analysis was performed under white-light illumination (AM 1.5G, 100 mW cm^{-2}). Incident photon-to-current conversion efficiency (IPCE) spectra were collected under the illumination of monochromatic light from a xenon lamp coupled with a monochromator. The photocatalytic performance was evaluated by the photodegradation of Congo Red (CR) under light illumination from a xenon lamp (500 W with a light intensity of 400 mW cm^{-2}). The prepared thin films with a size of 5 × 5 mm were dipped into an aqueous solution (4 ml) of CR (4 mg l^{-1}). The CR solutions were analyzed with a UV–visible spectrophotometer to measure the concentration variation in the photodegradation of CR through recording the corresponding absorbance of the characteristic peak at 497 nm.

RESULTS AND DISCUSSION

The BVO–WO heterostructure films were prepared by pulsed laser deposition. Details of the growth can be found in the Methods section. To identify phases and determine the orientation relationship between phases in the heterostructure, XRD was employed. Based on the results of XRD $2\theta - \theta$ scans (Figure 2a), the out-of-plane lattice parameters of BVO and WO were 11.68 and 7.74 Å, respectively, which can be identified as family peaks of monoclinic BVO (00*l*) and orthorhombic WO (00*l*), respectively. In addition, only the diffraction peaks of BVO (00*l*) and WO (00*l*) can be detected, confirming no contributions came from other orientations or secondary phases. This observation suggests that the WO–BVO heterostructure on the YSZ (100) substrate spontaneously separated into two pure phases during deposition. The epitaxy relation was then revealed by in-plane Φ scans of BVO {013} and WO {022} reflections, as shown in the inset of Figure 2a. The four peaks, instead of the typical twofold symmetry of both monoclinic and orthorhombic structures, observed in the Φ scans, implies that both BVO and WO have two sets of structural domains, which are separated by a 90° rotation around the *c* axis. In addition, the peaks of BVO {013} align well with those of YSZ {022}, indicating that the *b* axis of BVO is parallel to the *b* axis of YSZ. On the other hand, the peaks of WO {022} appear at every 45° after YSZ {022}, implying that the *b* axis of WO is parallel to the diagonal direction of YSZ. Therefore, a heteroepitaxy of BVO–WO on YSZ with an in-plane orientation relationship is then suggested to be [010]$_{BVO}$// [110]$_{WO}$//[010]$_{YSZ}$.

Further investigation into the microstructure of the BVO–WO heteroepitaxy with a WO volume fraction (V_{WO}) of ~ 30% was performed by TEM. Figure 2b shows the cross-sectional TEM image taken along the [010]$_{YSZ}$ zone axis. Vertically aligned columnar

Figure 1 Illustration of the self-assembled BVO–WO nanocomposite.

Good optical absorption photocatalyst (BiVO$_4$)

Good charge transport photocatalyst (WO$_3$)

Single crystal substrate

Figure 2 Structure characterization of the BVO–WO nanocomposite. (**a**) XRD $2\theta - \theta$ scans of pure WO, BVO and the BVO–WO nanocomposite showing only (00*l*)-type peaks of WO and BVO. Inset shows XRD ϕ scans of YSZ {022}, BVO {013} and WO {022} reflections for the BVO–WO heterostructure. (**b**–**e**) Cross-sectional TEM images of the BVO–WO nanocomposite taken along the [010]$_{YSZ}$ zone axis. Magnified images taken from the marked areas on (**d**) BVO and (**e**) WO, showing their out-of-plane and in-plane d-spacing parameters. (**f**) X-ray reciprocal space maps (RSMs) of the BVO–WO composite grown on ITO/YSZ. (**g**) Schematic representation of in-plane structure of BVO–WO heteroepitaxy grown on an ITO buffer layer and YSZ (001) substrate.

structures can be clearly observed. The high-resolution TEM images (Figures 2c–e) reveal the phase separation of BVO and WO, which is in an excellent agreement with the XRD analyses. The in-plane and out-of-plane lattice parameters of the BVO ($d_{200} = 2.53$ Å, $d_{002} = 5.81$ Å) and WO ($d_{220} = 2.62$ Å, $d_{002} = 3.86$ Å) phases are in good agreement with the lattice constants of the bulk ($a = 5.196$ Å, $b = 5.094$ Å, $c = 11.705$ Å, $\beta = 90.38°$) for monoclinic BVO and for orthorhombic WO ($a = 7.341$ Å, $b = 7.570$ Å, $c = 7.754$ Å).[17] The surface morphology of the WO–BVO heterostructures was explored through scanning electron microscopy. Supplementary Figure S1 clearly shows that there are many bamboo-like structures randomly distributed on the atomically flat surface. An atomically flat BVO film can be expected due to the small lattice mismatch (~1%) between monoclinic BVO and YSZ ($a = 5.145$ Å), as shown in the image (Supplementary Figure S2) and characterized by atomic force microscopy. Meanwhile, the density of the bamboo-like structures increased with V_{WO} and thus we can conclude that the bamboo-like structures are WO nanocrystals embedded in the BVO matrix. Therefore, V_{WO} can be regarded as a control parameter to tune the interface-to-volume ratio in the WO mesocrystal-embedded BVO system. To study the PEC performance of the heterostructures, a bottom electrode should be inserted between the substrate and heterostructure. A conducting layer of ITO was deposited, because it has a good lattice match to BVO, WO and YSZ. The topographic atomic force microscopy image of the ITO/YSZ sample (Supplementary Figure S3)

reveals an atomically flat surface with root-mean-square roughness values of ~0.6 nm. XRD $2\theta - \theta$ scans, in-plane Φ scans and TEM data (Supplementary Figures S4 and S5) clearly show the phase separation and the epitaxial relationships among the nanopillars, matrix, buffer layer and substrate. In addition, X-ray reciprocal space maps around the (202) diffraction of the YSZ substrate were recorded to analyze the structural information of all constituents in this nanocomposite system. As shown in Figure 2f, three additional diffraction peaks located at (2.002 0 2.043), (1.99 0 1.764) and (1.968 0 2.676) can be identified as ITO (404), BVO (204) and WO (224) reflections, respectively, clearly indicating that all phases are spontaneously separated and in good epitaxial relationship with the YSZ substrate. According to these peak positions, the corresponding lattice parameters are $a = b = 10.286$ Å and $c = 10.08$ Å for ITO, $a \approx b = 5.174$ Å and $c = 11.674$ Å for BVO and $a \approx b = 7.39$ Å and $c = 7.696$ Å for WO. These results confirmed that the epitaxial BVO–WO heterostructure was not changed even when an ITO buffer layer was added. The in-plane structural relationships of the BVO–WO heterostructure grown on an ITO buffer layer and on a YSZ substrate are further summarized in the schematic in Figure 2g. The photoactive facets of BVO and WO were fabricated to be (001) with the interface relationship of BVO (100)–WO (110) and BVO (010)–WO (1–10), providing a well-controlled system to understand charge interaction and its correlation to PEC performance.
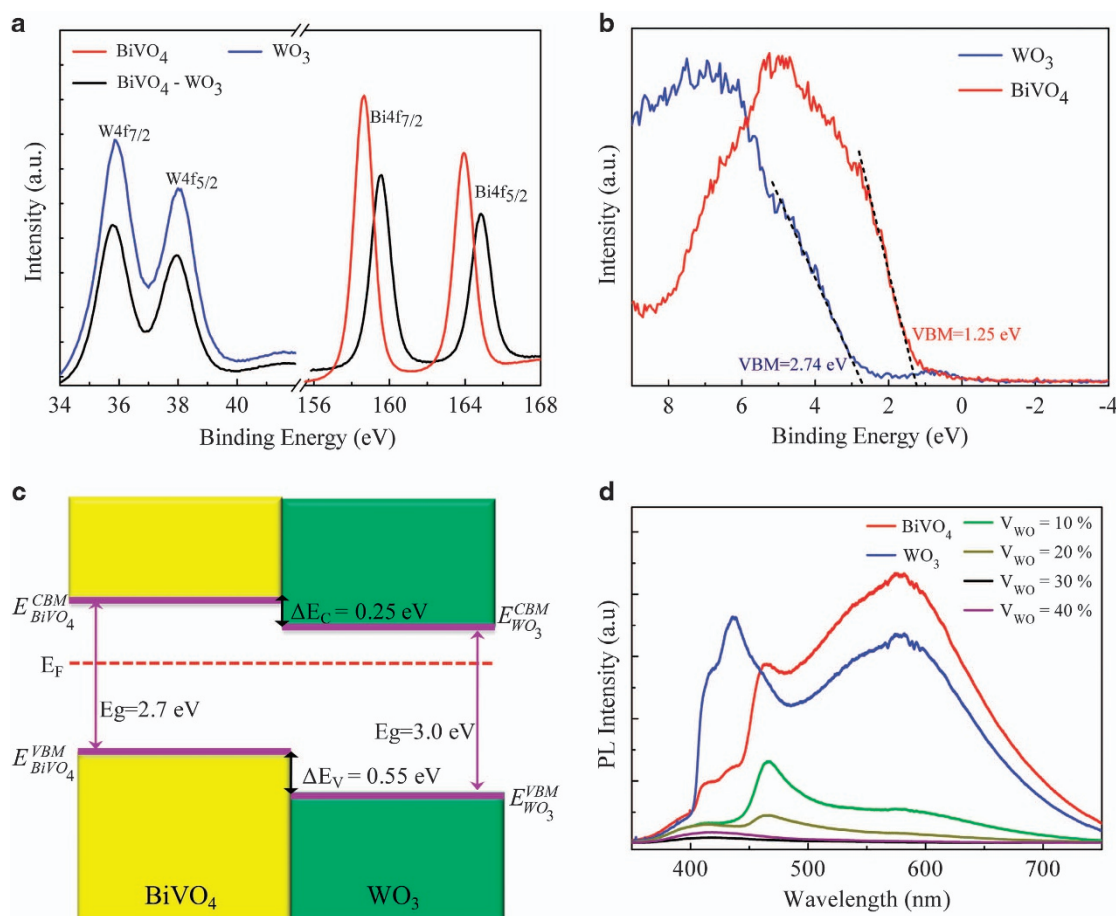
Figure 3 Band alignment between WO and BVO determined by XPS: (**a**) W$_{4f}$ and Bi$_{4f}$ XPS spectra of pure WO, pure BVO and a typical BVO–WO nanocomposite. (**b**) VB spectra of pure BVO and WO. (**c**) Band alignment of the BVO–WO heterojunction. E^{VBM} is the VBMs, E^{CBM} is the CB minima and ΔE_V and ΔE_C are the VB and CB offset, respectively. (**d**) PL spectra of pure BVO, pure WO and the nanocomposites with various V_{WO} ratios at 10 K.

With the establishment of the structural nature of the WO mesocrystal-embedded BVO system, it is important to characterize the electronic structure of the heterojunction. The optical responses of the pure BVO, pure WO and BVO–WO heterostructures were studied with UV–visible absorption spectroscopy. As shown in Supplementary Figure S6, the two pure samples showed absorption edges attributable to the corresponding bandgap absorption. For the BVO–WO heterostructures, there was a blue-shift in the absorption edge compared with that of pure BVO. With a further increase in V_{WO}, the absorption edge of BVO–WO shifted to a much shorter wavelength, reflecting the increased contribution of WO. Notably, an enhanced absorbance in the near-UV region was observed for all three BVO–WO heterostructures. This phenomenon suggested that more photons can be harvested due to the improved light absorption, which may help to enhance the photoconversion efficiency for BVO–WO. The optical bandgaps of pure BVO and WO were extracted to be 2.7 and 3.0 eV. XPS was further conducted to determine the band alignment of the BVO–WO heterojunction. Figure 3a shows the Bi 4f and W 4f core levels of pure BVO, pure WO and the WO mesocrystal-embedded BVO sample. In the heterostructure, the Bi 4f core level shifts towards higher binding energy, whereas the W 4f core level shifts towards lower binding energy. Determined by linear extrapolation of the leading edge of the valence band (VB) spectra, as shown in Figure 3b, the values of the VB maxima (VBMs) of the pure BVO and WO films

are 1.25 and 2.74 eV, respectively. As the zero point of the binding energy corresponds to the Fermi level, the value of the VBM can be used to estimate the position of the Fermi level within the bandgap. The Fermi level of pure BVO is located close to the middle of its energy gap, because its VBM value is equal to half of its bandgap. On the other hand, with a VBM value of 2.74 eV and a bandgap value of 3 eV, the Fermi level of pure WO is very close to its conduction band (CB). The VB offset (E_{VBO}) and CB offset (E_{CBO}) of the BVO–WO heterojunction calculated using Kraut's method[18] are 0.55 and 0.25 eV, respectively. Based on this result, we can construct a schematic to illustrate the energy band diagram of the BVO–WO heterojunction, as shown in Figure 3c, in which the VBM of WO lies 0.55 eV below that of BVO and the CB minimum of WO lies 0.25 eV below that of BVO. According to this band structure, one should expect an enhancement in charge separation, as photoexcited electrons should move from BVO to WO, whereas photogenerated holes could easily flow from WO to BVO. Such an enhancement should lead to a significant suppression of electron-hole (exciton) recombination and result in a great enhancement in the photoactivity. To investigate the existence of this charge separation, we carried out PL measurements. Figure 3d shows the PL spectra of pure BVO, pure WO and the BVO-WO nanocomposites with various V_{WO} at 10 K. The PL peaks at ~ 430 and 465 nm are attributed to the near-band-edge emissions of pure WO and BVO, respectively. The broad emissions at long wavelengths can

be ascribed to recombinations from *O*-related defects, such as *O* clustering, vacancy and alloy fluctuations. Interestingly, the emission intensity of both samples within the heterostructures quenches significantly with increasing V_{WO}. These facts indicate that the processes of photogenerated carrier recombination in both BVO and WO are suppressed markedly. Accordingly, the aforementioned PL quenching effect in the heterostructures suggests that the photoexcited charges transfer across the heterointerface and result in an efficient separation of electrons and holes in the heterojunction.

To probe the dynamics of photoexcited electrons in the composites, time-resolved photoinduced reflectivity change ($\Delta R/R$) transient spectroscopy was employed. Figure 4a shows the typical curves of time-resolved photoinduced $\Delta R/R$ in pure BVO, pure WO and the

BVO–WO heterostructures with different V_{WO}. In pure BVO, after photon excitation by a pump pulse with a photon energy of 3.1 eV, the $\Delta R/R$ swiftly rises at zero delay time due to optical transitions across the bandgap of BVO with the generation of electrons in the CB and holes in the VB.[19] These high-energy quasiparticles accumulated in the V_{3d} CB further release their energy through phonons, that is, the oscillation feature observed in $\Delta R/R$. According to previous studies on Au/BVO heterostructures,[20] we know that the oscillating components are due to coherent phonons generated by electronic excitation from pump pulses in BVO, as shown by the Fourier power spectrograms in Figure 4b. Two dominating peaks with frequencies of 0.030 and 0.045 THz were clearly found. However, we cannot observe the same oscillation signals in pure WO (see Figures 4a and b). Only sub-ps and hundred-ps relaxation dynamics were revealed in pure WO. It is remarkable that not only the relaxation dynamics but also the oscillation signals with 0.030 and 0.045 THz are strongly suppressed by increasing V_{WO} from 0 to 10%. These results indicate that the photoexcited carriers in BVO transfer from BVO to WO across the heterointerface.[21] Interestingly, the amplitude of the oscillation signals is significantly raised upon further increasing V_{WO} to 20% (see Figures 4b and c), which implies that the charge-transfer efficiency across the heterointerface would not be enhanced more by further increasing the interface-to-volume ratio. Consequently, $V_{WO} = 10\%$ is the optimal value for charge-transfer efficiency in the BVO–WO heterostructures.

Low charge-transfer resistance at the photoanode-electrolyte interface is a critical factor for an efficient photoanode. To investigate the charge-transfer kinetics of the photoanode composed of the WO mesocrystal-embedded BVO system, EIS was carried out under simulated solar light illumination. Figure 5a shows the EIS spectra presented in the Nyquist diagram for pure BVO, pure WO and BVO–WO heterostructures with various V_{WO}. The PEC process occurring at the electrode-electrolyte interface can be presented in terms of the equivalent Randle circuit model, as shown in the inset of Figure 5a. In this model, R_s is the electrolyte resistance, C_{dl} is the capacitance phase element and R_{ct} is the charge-transfer resistance at the electrode–electrolyte interface. A smaller R_{ct} corresponds to better charge-transfer efficiency, thus resulting in the improved photoactivity of the electrode. The fitted R_{ct} value for the pure WO sample (793 Ω) is much smaller than that for the pure BVO sample (24 000 Ω), indicating the charge-transfer efficiency of WO is much better than that of BVO. For the BVO–WO heterostructures, the R_{ct} values were
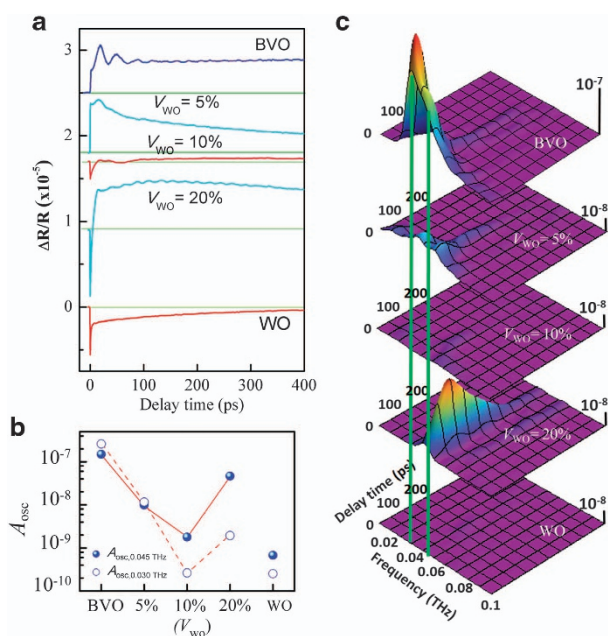
Figure 4 Ultrafast time-resolved photoinduced reflectivity change ($\Delta R/R$) transient spectroscopy. (**a**) The typical $\Delta R/R$ curves in pure BVO, pure WO and the BVO–WO heterostructures with different percentages of WO (V_{WO}). (**b**) Fourier power spectrograms obtained from the $\Delta R/R$ curves in **a**. (**c**) Amplitude of oscillation A_{osc} with 0.03 and 0.045 THz in **b** as a function of percentage of WO (V_{WO}). The solid and dashed lines are guides for the eyes.
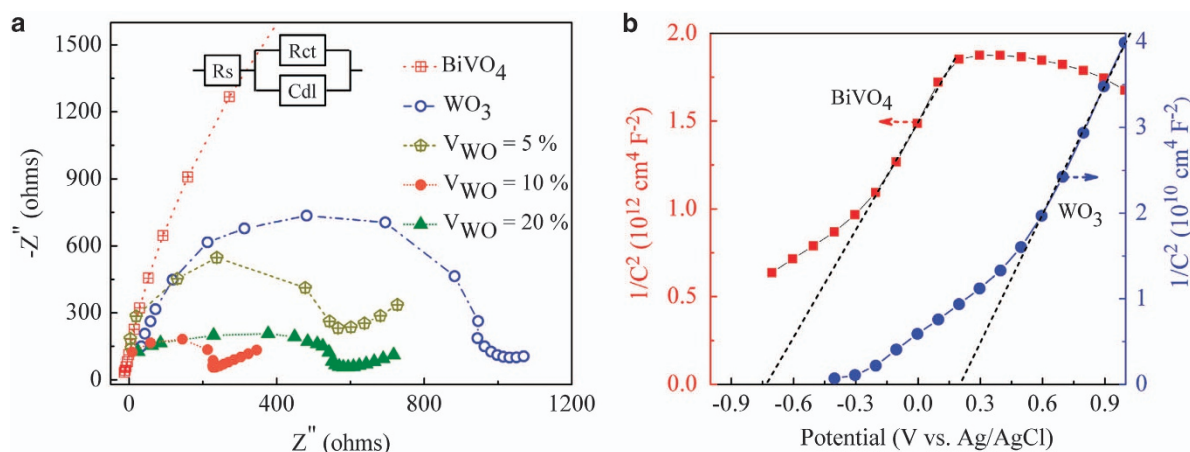

Figure 5 (**a**) Nyquist plots and (**b**) Mott–Schottky plots for the WO, BVO and BVO–WO photoelectrodes in 0.5 M Na₂SO₄ solution under AM 1.5 illumination.

6

sharply reduced to 663, 184 and 341 Ω with respect to $V_{WO} = 20\%$, 10% and 5%, respectively. In the BVO–WO heterostructures, the BVO matrix serves as the light absorber due to its narrow bandgap and the WO mesocrystal acts as an electron conductor owing to its good charge-transfer properties. Under light excitation, photogenerated electrons can move from the CB of BVO to that of WO and are subsequently transported toward the external circuit through the underlying ITO. On the other hand, the photogenerated holes delocalized in BVO move to the electrode/electrolyte interface to drive the redox reaction, leading to a smaller R_{ct}. Consequently, we can conclude that the vertical heterojunction of the BVO–WO system with a high interface-to-volume ratio suppressed electron-hole recombination and improved the charge-transfer efficiency significantly. Furthermore, the Mott–Schottky plots collected from the pure BVO and WO samples at a frequency of 1 kHz under light illumination (100 mW cm^{-2}) are presented in Figure 5b. The slope of the plots has an inverse relationship with the carrier density in the semiconductor film. The carrier densities of the pure BVO and WO electrodes can be estimated using the Mott–Schottky equation.[22] With ε-values of 300 for WO[23] and 180 for BVO,[24] the carrier densities of the pure WO and BVO samples under light excitation were estimated to be 9.68×10^{18} and 4.03×10^{17} cm^{-3}, respectively. The higher carrier density of WO is consistent with its better charge-transfer characteristics. In addition, the

flat-band potential of the pure photoanodes under light illumination can be estimated by taking the x-intercept of a linear fit to the Mott–Schottky plot as a function of applied potential. With the assumption that the flat-band potential lies at the same potential as that of the CB edge,[25] and by subtracting the optical bandgap value from the CB level, the band alignment between BVO and WO was constructed, as shown in Supplementary Figure S7. Such a staggered band alignment would give rise to electron accumulation at the CB of WO and hole concentration at the VB of BVO, which was fundamentally consistent with the results deduced from the XPS measurement.

To reveal the essential correlation between the electrical characterization and photoactivities of the WO mesocrystal-embedded BVO film, the photocatalytic degradation of organic contaminants and the PEC water oxidation were performed. Photocatalytic degradation was examined by monitoring the relationship between the degradation rate of CR and the light irradiation time, catalyzed by pure BVO, pure WO and the BVO–WO heterostructure, as shown in Supplementary Figure S8. The results clearly show that the BVO–WO heterostructure exhibits higher degradation ability than either pure BVO or WO. In fact, both photocatalytic oxidation by semiconductor nanomaterials and photosensitized oxidation by dye molecules can occur during visible-light irradiation.[26,27] It was difficult to separate the contribution of CR sensitization from the overall photocatalytic performance. It
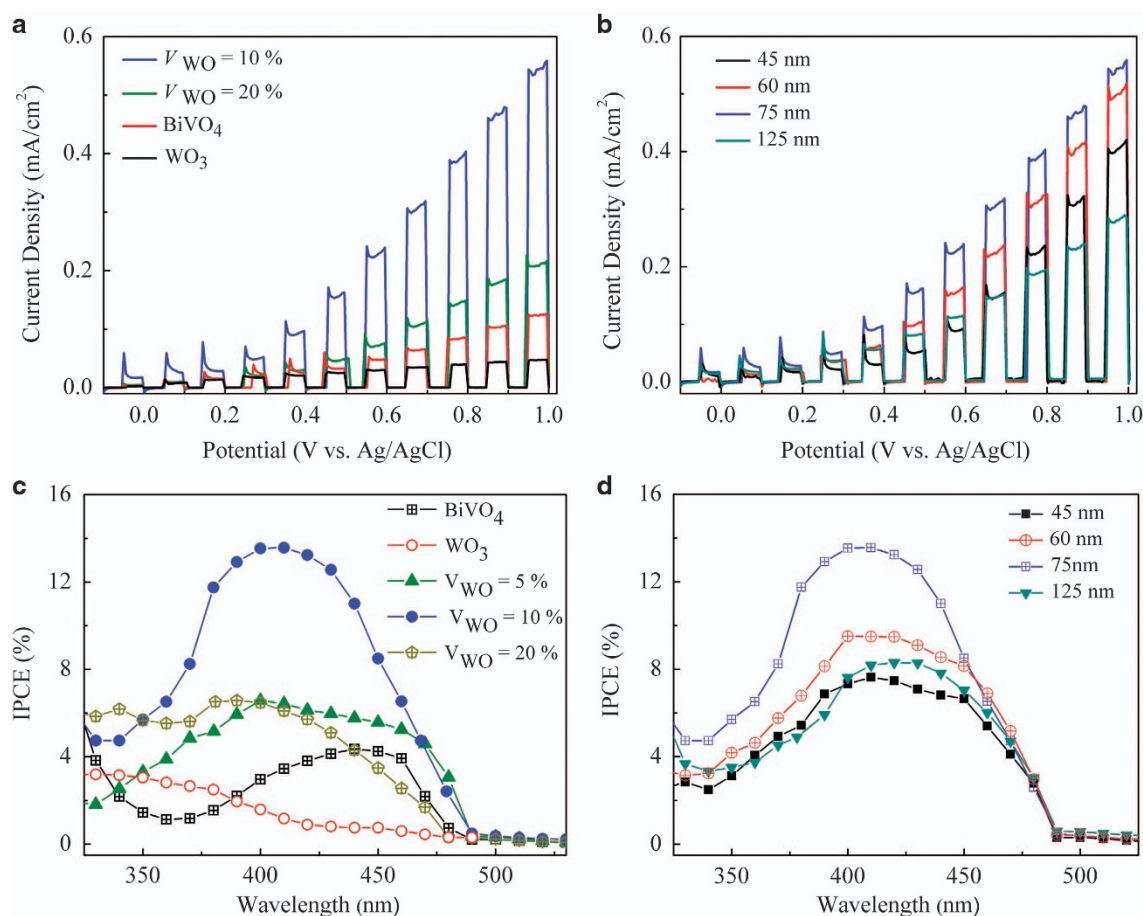
Figure 6 Photoelectrochemical performance of the BVO–WO photoanode in 0.5 M Na$_2$SO$_4$ electrolyte. Current–voltage (*J–V*) curves (**a**) the BVO–WO nanocomposites with various V_{WO} ratios and (**b**) the BVO–WO nanocomposites with $V_{WO} = 10\%$ with different thicknesses. (**c,d**) IPCE of BVO–WO nanocomposites with various V_{WO} ratios and different thicknesses, respectively. The *J–V* measurements were recorded under simulated AM 1.5G illumination. The IPCE was measured at 0.6 V versus Ag/AgCl.

should be noted however that experimental conditions, such as sample size, CR concentration, pH value and reaction temperature, were identical for all tested electrodes, meaning that the dye sensitization effect was universal among the different samples. Thus, the significantly enhanced photoactivity of the BVO–WO heterostructure is a major contributor to photocatalysis due to the narrow optical gap of BVO and the enhanced interfacial charge transfer and separation. Furthermore, the PEC performance of the BVO–WO photoelectrodes was investigated by measuring the photocurrent density–voltage (J–V) curve and the IPCE under simulated AM 1.5G illumination in aqueous 0.5 M Na_2SO_4. Figure 6a presents the J–V curves of pure BVO, pure WO and heterostructures with various V_{WO}. To make the results consistent, the thickness of all samples was kept the same at ~ 75 nm. The photocurrents of the heterostructured samples increased rapidly with applied anodic potential compared to that of the pure BVO and WO samples. The $V_{WO} = 10\%$ heterostructured photoelectrode exhibited the highest photocurrent of 0.57 mA cm^{-2} at 1 V (vs Ag/AgCl). The thickness dependence of the PEC performance was further investigated on samples with $V_{WO} = 10\%$, as shown in Figure 6b. By increasing the thickness from 45 to 75 nm, the photocurrent was enhanced; however, a further increase in the thickness to 125 nm results in a decrease in the photocurrent. The optimal thickness of the electrodes is ~ 75 nm, which is approximately close to the hole diffusion length (70–100 nm) in BVO films.[28,29]

Figures 6c and d show the IPCE spectra of the heterostructured electrodes together with pure BVO and WO samples measured at 0.6 V (vs Ag/AgCl) in 0.5 M Na_2SO_4. The IPCE spectra show onsets at ~ 485 and 450 nm for the pure BVO and WO samples, respectively, which are in an agreement with their bandgaps. In addition, all the heterostructured electrodes showed an onset of IPCE at the same wavelength as the pure BVO sample. As WO cannot absorb light with wavelengths between 400 and 500 nm, the IPCE of the BVO–WO heterostructures in this range is mainly contributed by the BVO matrix. The IPCE of all heterostructured electrodes was higher than that of the pure BVO and WO samples, which is consistent with the J–V curves shown in Figure 6a. This enhancement is attributed to the formation of the heterojunction between the light-absorber BVO and the good charge-transfer material WO. In this heterojunction, the photogenerated electrons in BVO move to WO rapidly and then the photoexcited holes transfer to the electrode/electrolyte interface for photoreaction.

CONCLUSION

We fabricated heterostructures composed of WO mesocrystals embedded in an epitaxial BVO matrix with well-defined crystal facets and interfaces between the WO and BVO phases as templates for the fundamental understanding of photoactivity in the nanocomposites. The heteroepitaxy, morphology and structure correlation between the WO mesocrystal and BVO matrix were characterized via a combination of XRD, scanning electron microscopy and TEM. XPS, PL spectroscopy, ultrafast dynamics analysis and EIS were used to reveal the band alignment at the heterointerface and characterize the charge transfer at the interface between the photoelectrode and electrolyte of the desired heterostructure. The band structure leads to a great enhancement in charge separation and the suppression of carrier recombination, resulting in a significant enhancement in the photoactivity. The tunable features and improved photoactivity of the mesocrystal-embedded heteroepitaxy provide a platform to understand the charge interaction between materials, as well as a new paradigm for the design of PEC cells with high efficiency.

CONFLICT OF INTEREST

The authors declare no conflict of interest.

1 Grätzel, M. Photoelectrochemical cells. *Nature* **414**, 338–344 (2001).
2 Walter, M. G., Warren, E. L., McKone, J. R., Boettcher, S. W., Mi, Q., Santori, E. A. & Lewis, N. S. Solar water splitting cells. *Chem. Rev.* **110**, 6446–6473 (2010).
3 Kamat, P. V. Photochemistry on nonreactive and reactive (semiconductor) surfaces. *Chem. Rev.* **93**, 267–300 (1993).
4 Reza Gholipour, M., Dinh, C.-T., Béland, F. & Do, T.-O. Nanocomposite heterojunctions as sunlight-driven photocatalysts for hydrogen production from water splitting. *Nanoscale* **7**, 8187–8208 (2015).
5 Liu, G., Yu, J. C., Lu, G. Q. M. & Cheng, H.-M. Crystal facet engineering of semiconductor photocatalysts: motivations, advances and unique properties. *Chem. Commun.* **47**, 6763–6783 (2011).
6 Zhang, R., Li, F., Wang, D., Yang, J., Li, M., Zhu, J., Zhou, X., Han, H. & Li, C. Spatial separation of photogenerated electrons and holes among {010} and {110} crystal facets of BiVO₄. *Nat. Commun.* **4**, 1–7 (2013).
7 Pan, J., Liu, G., Lu, G. Q. M. & Cheng, H.-M. On the true photoreactivity order of {001}, {010}, and {101} facets of anatase TiO2 crystals. *Angew. Chem. Int. Ed. Engl.* **50**, 2133–2137 (2011).
8 Fang, J., Ding, B. & Gleiter, H. Mesocrystals: syntheses in metals and applications. *Chem. Soc. Rev.* **40**, 5347–5360 (2011).
9 Zhou, L. & O'Brien, P. Mesocrystals: a new class of solid materials. *Small* **4**, 1566–1574 (2008).
10 Yang, J. C., He, Q., Zhu, Y. M., Lin, J. C., Liu, H. J., Hsieh, Y. H., Wu, P. C., Chen, Y. L., Lee, S. F., Chin, Y. Y., Lin, H.-J., Chen, C. T., Zhan, Q., Arenholz, E. & Chu, Y. H. Magnetic mesocrystal-assisted magnetoresistance in manganite. *Nano Lett.* **14**, 6073–6079 (2014).
11 Prévot, M. S. & Sivula, K. Photoelectrochemical tandem cells for solar water splitting. *J. Phys. Chem. C* **117**, 17879–17893 (2013).
12 Kim, T. W. & Choi, K.-S. Nanoporous BiVO₄ Photoanodes with dual-layer oxygen evolution catalysts for solar water splitting. *Science* **343**, 990–994 (2014).
13 Bignozzi, C. A., Caramori, S., Cristino, V., Argazzi, R., Meda, L. & Tacca, A. Nanostructured photoelectrodes based on WO₃: applications to photooxidation of aqueous electrolytes. *Chem. Soc. Rev.* **42**, 2228–2246 (2013).
14 Rao, P. M., Cai, L., Liu, C., Cho, I. S., Lee, C. H., Weisse, J. M., Yang, P. & Zheng, X. Simultaneously efficient light absorption and charge separation in WO₃/BiVO₄ core/shell nanowire photoanode for photoelectrochemical water oxidation. *Nano Lett.* **14**, 1099–1105 (2014).
15 Pihosh, Y., Turkevych, I., Mawatari, K., Asai, T., Hisatomi, T., Uemura, J., Tosa, M., Shimamura, K., Kubota, J., Domen, K. & Kitamori, T. Nanostructured WO₃/BiVO₄ photoanodes for efficient photoelectrochemical water splitting. *Small* **10**, 1–8 (2014).
16 Hong, S. J., Lee, S., Jang, J. S. & Lee, J. S. Heterojunction BiVO₄/WO₃ electrodes for enhanced photoactivity of water oxidation. *Energy Environ. Sci.* **4**, 1781–1787 (2011).
17 Park, Y., McDonald, K. J. & Choi, K.-S. Progress in bismuth vanadate photoanodes for use in solar water oxidation. *Chem. Soc. Rev.* **42**, 2321–2337 (2013).
18 Kraut, E. A., Grant, R. W., Waldrop, J. R. & Eowalczyk, S. P. Precise determination of the valence band edge in X-Ray photoemission spectra: application to measurement of semiconductor interface potentials. *Phys. Rev. Lett.* **44**, 1620–1623 (1980).
19 Zhao, Z., Li, Z. & Zou, Z. Electronic structure and optical properties of monoclinic clinobisvanite BiVO₄. *Phys. Chem. Chem. Phys.* **13**, 4746–4753 (2011).
20 Chien, N. V., Chang, W. S., Chen, J. W., Tsai, K. A., Tzeng, W. Y., Lin, Y. C., Kuo, H. H., Liu, H. J., Chang, K. D., Chou, W. C., Wu, C. L., Chen, Y. C., Luo, C. W., Hsu, Y. J. & Chu, Y. H. Heteroepitaxial approach to explore charge dynamics across Au/BiVO₄ interface for photoactivity enhancement. *Nano Energy* **15**, 625–633 (2015).
21 Grigioni, I., Stamplecoskie, K. G., Selli, E. & Kamat, P. V. Dynamics of photogenerated charge carriers in WO₃/BiVO₄ heterojunction photoanodes. *J. Phys. Chem. C* **119**, 20792–20800 (2015).
22 Parmar, K. P. S., Kang, H. J., Bist, A., Dua, P., Jang, J. S. & Lee, J. S. Photocatalytic and photoelectrochemical water oxidation over metal-doped monoclinic BiVO₄ photoanodes. *Chem. Sus. Chem.* **5**, 1926–1934 (2012).
23 Xu, F., Yao, Y., Bai, D., Xu, R., Mei, J., Wu, D., Gao, Z. & Jiang, K. Au nanoparticle decorated WO₃ photoelectrode for enhanced photoelectrochemical properties. *RSC Adv* **5**, 60339–60344 (2015).
24 Sarkar, S., Das, N. S. & Chattopadhyay, K. K. Optical constants, dispersion energy parameters and dielectric properties of ultra-smooth nanocrystalline BiVO₄ thin films prepared by Rf-magnetron sputtering. *Solid State Sci.* **33**, 58–66 (2014).
25 Premkumar, J. Development of super-hydrophilicity on nitrogen-doped TiO₂ thin film surface by photoelectrochemical method under visible light. *Chem. Mater.* **16**, 3980–3981 (2004).

8

26 Konstantinou, I. K. & Albanis, T. A. TiO₂-assisted photocatalytic degradation of azo dyes in aqueous solution: kinetic and mechanistic investigations. *Appl. Catal. B Environ.* **49**, 1–14 (2004).

27 Ajmal, A., Majeed, I. & Malik, N. Principles and mechanisms of photocatalytic dye degradation on TiO 2 based photocatalysts: a comparative overview. *RSC Adv.* **4**, 37003–37026 (2014).

28 Abdi, F. F., Savenije, T. J., May, M. M., Dam, B. & Van De Krol, R. The origin of slow carrier transport in BiVO₄ thin film photoanodes: a time-resolved microwave conductivity study. *J. Phys. Chem. Lett.* **4**, 2752–2757 (2013).

29 Rettie, A. J. E., Lee, H. C., Marshall, L. G., Lin, J.-F., Capan, C., Lindemuth, J., McCloy, J. S., Zhou, J., Bard, A. J. & Mullins, C. B. Combined charge carrier transport and photoelectrochemical characterization of BiVO₄ single crystals: intrinsic behavior of a complex metal oxide. *J. Am. Chem. Soc.* **135**, 11389–11396 (2013).

Supplementary Information accompanies the paper on the NPG Asia Materials website (http://www.nature.com/am)